1-1-2016

Significant enhancement of the cycling performance and rate capability of the P/C composite via chemical bonding (P-C)

Weijie Li
University of Wollongong, wl347@uowmail.edu.au

Shulei Chou
University of Wollongong, shulei@uow.edu.au

Jiazhao Wang
University of Wollongong, jiazhao@uow.edu.au

Hua-Kun Liu
University of Wollongong, hua@uow.edu.au

S X. Dou
University of Wollongong, shi@uow.edu.au

Significant enhancement of the cycling performance and rate capability of the P/C composite via chemical bonding (P-C)

Abstract

Among anode materials for sodium ion batteries, red phosphorus is a very promising one due to its abundant reserves, low-cost and high theoretical capacity of 2600 mA h g-1. However, its huge volume expansion on sodiation (~490%) and poor conductivity leads to dramatic capacity decay, restraining its practical application. To improve the electrochemical performance, here, we prepared a red phosphorus and graphene nanoplate composite using cheap red P and natural graphite as the starting materials via a simple and scalable ball-milling method. The phosphorus-carbon bond formed during the milling process improves the electrical connectivity between P particles and graphene nanoplates, consequently stabilizing the structure of the composite to achieve high cycling performance and rate capability. As a result, the red phosphorus and graphene nanoplate composite delivered a high reversible capacity of 1146 mA h g-1 (calculated on the basis of the composite mass) at a current density of 100 mA g-1 and an excellent cycling stability of 200 cycles with 92.5% capacity retention.

Keywords

chemical, via, composite, c, p, capability, bonding, rate, significant, performance, cycling, enhancement

Disciplines

Engineering | Physical Sciences and Mathematics

Publication Details

Li, W., Chou, S., Wang, J., Liu, H. & Dou, S. (2016). Significant enhancement of the cycling performance and rate capability of the P/C composite via chemical bonding (P-C). Journal of Materials Chemistry A, 4 (2), 505-511.

Journal of Materials Chemistry A

PAPER

View Article Online
View Journal | View Issue

CrossMark click for updates

Cite this: J. Mater. Chem. A, 2016, 4, 505

Significant enhancement of the cycling performance and rate capability of the P/C composite *via* chemical bonding (P–C)†

Wei-Jie Li, Shu-Lei Chou,* Jia-Zhao Wang, Hua-Kun Liu and Shi-Xue Dou

Received 26th October 2015
Accepted 13th November 2015

DOI: 10.1039/c5ta08590j

www.rsc.org/MaterialsA

Among anode materials for sodium ion batteries, red phosphorus is a very promising one due to its abundant reserves, low-cost and high theoretical capacity of 2600 mA h g^{-1}. However, its huge volume expansion on sodiation (~490%) and poor conductivity leads to dramatic capacity decay, restraining its practical application. To improve the electrochemical performance, here, we prepared a red phosphorus and graphene nanoplate composite using cheap red P and natural graphite as the starting materials *via* a simple and scalable ball-milling method. The phosphorus–carbon bond formed during the milling process improves the electrical connectivity between P particles and graphene nanoplates, consequently stabilizing the structure of the composite to achieve high cycling performance and rate capability. As a result, the red phosphorus and graphene nanoplate composite delivered a high reversible capacity of 1146 mA h g^{-1} (calculated on the basis of the composite mass) at a current density of 100 mA g^{-1} and an excellent cycling stability of 200 cycles with 92.5% capacity retention.

1. Introduction

Sodium ion batteries (SIBs), as a promising alternative to lithium ion batteries, which might well lead to a new era in energy storage systems, have attracted increasing attention, owing to the abundant sodium resources around the world and sodium's similar electrochemical (or physical) properties to lithium.[1–10] The big challenge for developing SIBs, however, is to search for an appropriate candidate with both a long lifetime and high capacity. In the case of cathode materials, a massive improvement of cycle life has now been achieved. $Na_3V_2(PO_4)_3$ and acetylene carbon composites delivered 97.0 mA h g^{-1} capacity with a retention of 96.4% over 200 cycles.[11] $Na_{1.25}V_3O_8$ nanowires presented excellent cycling performance with 95% and 92% capacity retention after 200 and 1000 cycles, respectively.[12] Our group developed a Na-enriched $Na_{1+x}FeFe(CN)_6$ cathode material, showing a superior capacity retention of 97% over 400 cycles.[13] In contrast, apart from carbon materials, anode materials seldom possess excellent cycling stability with more than 80% capacity retention after 200 cycles. For example, N-doped carbon showed 88.7% capacity retention over 200 cycles,[14] and carbon nanofibers synthesized by electrospinning exhibited excellent cycling stability, with 97.7% capacity retention over 200 cycles.[15] One of the biggest drawbacks of carbon materials, however, is their low capacity (less than 300 mA h g^{-1}). In addition, Sn- and Sb-based materials, which can deliver 600 mA h g^{-1} capacity, based on their alloying mechanism, have recently demonstrated improved cycling performance.[16–19]

Among the anode candidates, red phosphorus has the highest theoretical capacity of ~2600 mA h g^{-1}, and it has been widely investigated since it was first reported as an anode material for SIBs in 2013.[20–22] The poor electrical conductivity and huge volume expansion (490%) of red phosphorus, however, result in its poor practical capacity and cycling stability, which are obstructing its practical application. To overcome these problems, various carbon materials, such as Super P®,[20,21] multi-walled carbon nanotubes (MWCNTs),[22] single-walled carbon nanotubes (SWCNTs),[23] and graphene,[24] have been introduced to prepare red phosphorus and carbon (P/C) composites, where the carbon plays roles in both improving the electrical conductivity and buffering the volume expansion. Compared with commercial red phosphorus, the cycling performance of P/Super P and P/MWCNT composites was improved to some extent, however, the capacity still gradually deteriorated. Among these P/C composites, P/SWCNT and phosphorus/graphene (P/G) composites showed improved cycling performance.[23,24] The P/SWCNT composite synthesized by the vaporization–condensation method showed excellent cycling stability with no capacity decay over 200 cycles at a current density of 500 mA g^{-1}.[23] There is a big potential safety hazard, however, if the tube is not well sealed, because of the white phosphorus generated during the preparation process at a temperature of 600 °C, and moreover, the utilization of SWCNTs can increase the cost. Song *et al.* reported that the P/G

Institute for Superconducting and Electronic Materials, University of Wollongong, 2522, Wollongong, Australia. E-mail: shulei@uow.edu.au

† Electronic supplementary information (ESI) available: XRD, SEM, Raman spectra and the electrochemical performance of the P/graphite-300 composite. See DOI: 10.1039/c5ta08590j

composite prepared *via* simple ball milling delivered 1706 mA h g^{-1} capacity (on the basis of phosphorus weight) with 95% retention of the capacity in the second cycle for over 60 cycles.[24] Such good cycling performance is proposed to originate from the strong P–O–C chemical bonds between the graphene nanosheets and the phosphorus, which can stabilize the solid electrolyte interphase (SEI) to improve the cycling performance. The preparation of graphene requires tedious steps, however, such as the synthesis of graphite oxide (GO) and the reduction of GO. Moreover, the price of graphene is higher than that of natural graphite. Previously, Jeon *et al.* reported that graphite can be exfoliated into graphene nanoplates during the ball milling process through the shear force.[25] Cui *et al.* demonstrated that the P–C bond can form during the ball-milling process to improve the contact between black phosphorus and carbon, giving the black phosphorus and carbon composite excellent electrochemical performance for lithium ion storage.[26]

Therefore, inspired by the reported functionality of the chemical P–C bond and the formation of graphene nanoplates from natural graphite during the ball-milling process, we chose the cheap graphite as the carbon source to prepare our chemically bonded red phosphorus and graphene nanoplate (P/GnP) composite as the anode for sodium ion batteries through the simple and productive ball-milling method. During the milling process, the bulk red phosphorus particles were milled into small nanoparticles and dispersed well into graphene nanoplates; such a reduction of particle size and the carbon matrix covering the phosphorus are conducive to reducing the volume expansion and buffering the stress from the volume expansion, respectively. Moreover, the formation of P–C bonds between red phosphorus and graphene nanoplates brings the graphene nanoplates into close contact with the P particles, maintaining the electrical contact between the P particles and the graphene nanoplates, and consequently, stabilizing the structure of the composite to improve its cycling performance. As a result, the P/GnP composite exhibits superior cycling performance for sodium ion storage, with 92.5% capacity retention over 200 cycles at a high current density of 1000 mA g^{-1}. Additionally, it shows excellent rate capability, retaining 274 mA h g^{-1} capacity, even when discharged at a high current density of 10 A g^{-1}, corresponding to 27.6% retention of the capacity delivered at 100 mA g^{-1}.

2. Experimental

2.1 Synthesis of the P/GnP composite

The red phosphorus (99%, Sigma Aldrich) and natural graphite were used as the raw materials without any further purification treatment. The P/GnP composite was prepared through a simple and productive ball-milling method. The weight ratio of red phosphorus to graphite was 7 : 3. Then, the materials were put into a jar and sealed in a glovebox under argon gas, which was followed by milling for 40 h at a speed of 500 rpm. The resultant composite was denoted as P/GnPs-500. To compare, a control sample was prepared under the same experimental conditions except the milling speed of 300 rpm, which is denoted as P/GnPs-300.

2.2 Material characterization

The microstructure of the powders was characterized by powder X-ray diffraction (XRD; GBC MMA diffractometer) with Cu K_α radiation at a scan rate of 2° min^{-1}. The morphology of the samples was investigated by field emission scanning electron microscopy (FESEM; JEOL JSM-7500FA) and scanning transmission electron microscopy (STEM, JEOL ARM200F) in conjunction with energy-dispersive X-ray spectroscopy (EDS). Raman spectra were collected using a JOBIN Yvon Horiba Raman spectrometer model HR800, with excitation using a 10 mW helium/neon laser at 632.8 nm in the range of 150 to 2000 cm^{-1}. FTIR spectra were performed by using a FTIR Prestige-21 (Shimadzu). X-ray photoelectron spectroscopy (XPS) was conducted using a SPECS PHOIBOS 100 Analyser installed in a high-vacuum chamber with a base pressure below 10^{-8} mbar, with X-ray excitation provided by Al K_a radiation with photon energy $h\nu = 1486.6$ eV at a high voltage of 12 kV and a power of 120 W. The XPS binding energy spectra were recorded at a pass energy of 20 eV in the fixed analyser transmission mode. Analysis of the XPS data was carried out using a commercial CasaXPS 2.3.15 software package. All the spectra were calibrated by C 1s = 284.6 eV.

2.3 Electrochemical test

The electrochemical measurements of the P/GnP composite as the anode material were conducted using 2032-type coin cells. The working electrode was prepared by coating an aqueous slurry containing 70 wt% active materials, 15 wt% Super-P® carbon black, and 15 wt% carboxymethyl cellulose (CMC) binder on a copper foil substrate. Then, the electrode film was dried in a vacuum oven at 80 °C overnight and pressed at 10 MPa. The electrodes were punched into disks with a loading of 1.5–2.0 mg cm^{-2}. The electrolyte used in this work was 1.0 mol L^{-1} $NaClO_4$ in an ethylene carbonate (EC) – diethyl carbonate (DEC) solution (1 : 1 v/v), with 5 wt% addition of fluoroethylene carbonate (FEC). All the cells were assembled in a glovebox filled with argon and tested at room temperature. The galvanostatic charge/discharge testing was conducted on a Biologic VMP3 electrochemical workstation with a cut-off voltage range from 0 to 1.5 V (*vs.* Na/Na^+). The rate capability of the P/GnP composite was also investigated at a variety of current densities from 50 mA g^{-1} to 10 A g^{-1} with a cut-off voltage range from 0 to 1.5 V (*vs.* Na/Na^+).

3. Results and discussion

The P/GnP composite was prepared by a simple and productive ball-milling method. Commercial red phosphorus and natural graphite were used as the starting materials, in the weight ratio of 7 : 3, respectively, and then milled at 500 rpm for 40 h under an argon atmosphere. The resultant composite was denoted as P/GnPs-500. The morphologies of the red phosphorus and graphite are shown in Fig. S1 in the ESI.† It is clear that the commercial red phosphorus is a micrometer-sized bulk and the graphite is a layered bulk (Fig. S1†). After milling, these two bulk materials were broken down into nanoscale particles ~100 nm

in size, as shown in Fig. 1(a) and (b), however, the morphology of graphite cannot be observed in the SEM images. To clearly detect the morphology of graphite in the P/GnP-500 composite, scanning transmission electron microscopy (STEM) was conducted. It is obvious that the graphite was exfoliated into nanoplates through the shear force during the milling process, and the small phosphorus particles were embedded in the graphene nanoplates (GnPs) (Fig. 1(c)). Moreover, the selected area electron diffraction (SAED, the inset of Fig. 1(c)) pattern shows a diffuse ring, suggesting that the P/GnPs-500 composite is amorphous. Energy-dispersive X-ray spectroscopy (EDS) mapping was carried out to further explore the structure of the P/GnPs-500 composite, as shown in Fig. 1(e) and (f). Significantly, the phosphorus was dispersed uniformly with the carbon, suggesting that the phosphorus and graphite were mixed uniformly and were in intimate contact.

To further investigate the connections between the phosphorus particles and the graphene nanoplates, a variety of characterization techniques, including powder X-ray diffraction (XRD), Raman spectroscopy, and X-ray photoelectron spectroscopy (XPS), were implemented. Fig. 2(a) shows the XRD patterns of the P/GnPs-500 composite and its precursors. The XRD pattern of the commercial red phosphorus shows broad and low-intensity peaks at 2θ of 15.5° and 32.3°, respectively, obviously indicating its amorphous nature. In the XRD pattern of graphite, there is a sharp diffraction peak at 26.5°, assigned to the (002) plane. After milling for 40 h, these diffraction peaks disappear, and no peak appears in the XRD pattern of the P/GnP composite. The XRD results demonstrate that the P/GnPs-500 composite is amorphous, consistent with the SAED pattern (inset of Fig. 1(c)). Raman spectra were collected to further test the structure of P/GnPs-500, as shown in Fig. 2(b). Red phosphorus shows three bands from 300 cm^{-1} to 500 cm^{-1}, assigned to the P–P bonds. For the P/GnP composite, these three bands were also observed, but their intensities were decreased, implying that some P–P bonds were broken up to generate the P–C bonds.[26] The spectrum of the graphite shows a weak D band at 1327 cm^{-1} and a strong G band at 1572 cm^{-1}, corresponding to the breathing mode of aromatic rings and the E_{2g} symmetrical bond stretching motion of pairs of C sp^2 atoms,

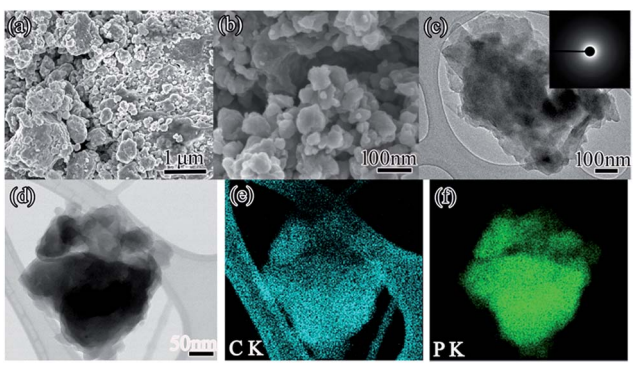

Fig. 1 Morphology of the P/GnP composite: (a) low and (b) high magnification SEM images; (c) and (d) STEM images (inset of (c) is the corresponding SAED pattern); element mapping corresponding to (d) of (e) carbon and (f) phosphorus in the P/GnP composite.

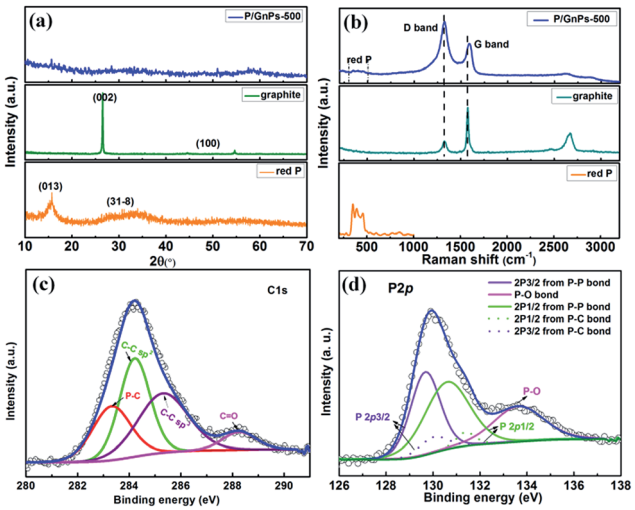

Fig. 2 Characterization of the P/GnPs-500 composite and its precursors: (a) XRD patterns; (b) Raman spectra; (c) high resolution C 1s XPS spectrum and (d) P 2p XPS spectrum of P/GnPs-500.

respectively.[27] Compared with the graphite, the intensity ratio of the D band to the G band (I_D/I_G) increased from 0.31 to 2.91 in the P/GnPs-500 composite, implying that the carbon in the composite was partially amorphous. Notably, a right shift of the G band from 1572 cm^{-1} for graphite to 1585 cm^{-1} was observed, demonstrating that the number of layers of graphite in the P/GnPs-500 composite was reduced due to the mechanical shear exfoliation of the graphite nanoplates.[27] XPS was carried out to detect the surface chemical composition of the P/GnPs-500 composite, and the XPS results are shown in Fig. 2(c) and (d). The C 1s peak is deconvoluted into four peaks at 283.4 eV, 284.6 eV, 285.3 eV and 288.3 eV (Fig. 2(c)). The peaks at 284.6 eV and 285.3 eV are assigned to the sp^2 and sp^3 C–C bond, respectively, while the peak at 288.2 eV is assigned to the C=O bond from the carbon. The peak at 283.7 eV should be ascribed to the P–C bond, according to J. Sun *et al.*[26] The P 2p spectrum is fitted to two pairs of $2p_{1/2}$ and $2p_{3/2}$ doublets, as shown in Fig. 2(d). One pair of $2p_{3/2}$ and $2p_{1/2}$ components at 129.7/130.6 eV corresponds to the P–P bond, while the other pair at 130.1/131.0 eV is assigned to the P–C bond, consistent with a previously reported result.[26] In addition, there is a fitting peak that appears at 133.9 eV, which is ascribed to the P–O bond. The appearance of the C=O and P–O bonds is possibly due to the oxidization of milled nanoparticles when the milling jars were opened. The XPS results demonstrate that P–C bonds are formed between red phosphorus and graphene nanoplates in the P/GnPs-500 composite.

To investigate the effects of milling speed on the structure of the P/GnP composite, we prepared a control sample under the same experimental conditions as for P/GnPs-500 except for using a milling speed of 300 rpm, with the sample denoted as P/GnPs-300. XRD, SEM, XPS, transmission electron microscopy (TEM), and Raman spectroscopy were carried out to characterize the P/GnPs-300, as shown in Fig. S2–S5.† The XRD pattern shows that there is no new phase emerging in the P/GnPs-300. The intensities of the peaks from graphite decreased after

milling compared with the pristine graphite, demonstrating that the particle size of the graphite in the composite had been reduced (Fig. S2†). From the SEM image, it is clear that the particle size of the P/GnPs-300 is about 100 nm. Moreover, the EDS mapping results indicate that the graphite and red P were mixed uniformly (Fig. S3(a)†). In the TEM image of P/GnPs-300, there are some lattice fringes with a spacing of ~0.34 nm, which were assigned to the gaps between the graphene layers in graphite (Fig. S3(b)†). This demonstrated that the extent of exfoliation of graphite in P/GnPs-300 is smaller than that of graphite in P/GnPs-500 (Fig. 1(c)). Fig. S4† shows the XPS spectra of P/GnPs-300. The C 1s peak is deconvoluted into two peaks at 284.6 eV and 288.3 eV assigned to the C–C bond and C–O, respectively, (Fig. S4(a)†). The P 2p spectrum is fitted to a pair of $2p_{3/2}$ and $2p_{1/2}$ components at 129.7/130.6 eV corresponding to the P–P bond. Besides that, there is a fitting peak that appears at 133.9 eV ascribed to the P–O bond, as shown in Fig. S4(b).† To clearly observe the structural differences between the P/GnPs-500 and P/GnPs-300, Raman spectroscopy was conducted, and the results are presented in Fig. S5.† For both the P/GnPs-500 and the P/GnPs-300 composites, the intensity of the D-band from carbon is larger than that of the G-band, suggesting that the graphite in the composites was partially amorphous after milling. In addition, compared with P/GnPs-300, the G-band in the P/GnPs-500 composite has left shifted from 1598 cm^{-1} to a lower wavenumber (1585 cm^{-1}). Considering the larger extent of exfoliation of graphite in P/GnPs-500, the G-band should shift to a large wavenumber, compared with the P/GnPs-300. However, the actual tendency is reverse. This is due to the P–C bond formation in the P/GnPs-500 composite through the π–p conjugation which makes the G-band shift left.[26] Therefore, the left shift of the G-band is also evidence of the P–C bond formation in the P/GnPs-500 composite. In addition, the FTIR spectra are also measured to test the P–C bond. The results show that there is an additional peak at 1006 cm^{-1} appearing in the FTIR spectrum of P/GnPs-500, compared with P/GnPs-300 (Fig. S6†), suggesting the formation of a new bond in the P/GnPs-500 composite. The formation of P–C bonds in the P/GnPs-500 composite provides good contact between red phosphorus particles and graphene nanoplates, consequently improving the electronic conductivity of red phosphorus and promoting structural integrity during sodiation/desodiation processes.

To validate the function of the P–C bonds in the P/GnP composites in the electrochemical performance, the P/GnP composites were tested in sodium ion half cells in the voltage range of 0–1.5 V. Both the capacity and the current density were calculated on the basis of the overall weight of the P/GnP composite. Fig. 3(a) shows the charge–discharge curves of the P/GnPs-500 and P/GnPs-300 composites in the first two cycles at a current density of 100 mA g^{-1}. In the discharge curves of both the P/GnPs-500 and the P/GnPs-300 composites, there are three sloping regions at 1.5–0.5 V, 0.5–0.25 V, and 0.25–0 V, respectively, corresponding to the multistep reaction between P and sodium to form the final Na_3P phase.[20–24] The P/GnPs-300 delivered a discharge capacity of 1376 and 822 mA h g^{-1} in the first and second cycles, respectively. Compared with the P/GnPs-300, the capacity delivered by the P/GnPs-500 composite is higher, with 1471 mA h g^{-1} capacity in the first cycle and 1146 mA h g^{-1} in the second cycle. Additionally, the hysteresis (ΔE) between the discharge and charge potential plateaus was reduced from 0.34 V for P/GnPs-300 to 0.22 V for P/GnPs-500. The reduced hysteresis is similar to that of the reported black phosphorus and graphene composite, which was proposed as evidence of P–C bond formation and consequently, improved coulombic efficiency resulting from the better connections between particles during the very large volume changes in the charge–discharge processes.[26] Both the increased capacity and the reduced hysteresis of the P/GnPs-500 composite demonstrate that it has better electronic conductivity than P/GnPs-300. The electrochemical impedance measurements also confirm this point, and the results are shown in Fig. S7.† Before testing the impedance, the cells were run for 5 cycles and then charged at 0.6 V. The impedance curves of both P/GnPs-500 and P/GnPs-300 show two semicircles in the medium frequency and low frequency regions, which could be assigned to the sodium ion diffusion through the solid electrolyte interphase (SEI) film (R_x) and the charge transfer resistance (R_{ct}), respectively. The R_{ct} was calculated using the equivalent circuit shown in Fig. S7(a).† Significantly, the R_{ct} value of the P/GnPs-500 composite (95 Ω) is very much smaller than that of the P/GnPs-300 (147 Ω), demonstrating that the electronic conductivity of the P/GnPs-500 composite is better than that of P/GnPs-300.

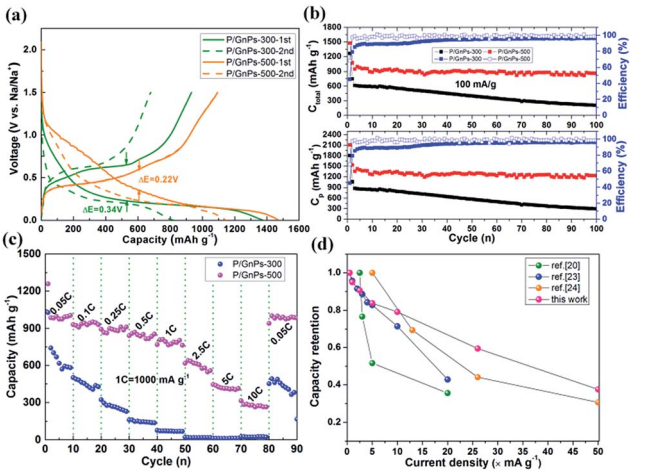

Fig. 3 Electrochemical performances of the P/GnPs-500 and P/GnPs-300 composites. (a) Charge–discharge curves of the P/GnP electrodes in the first two cycles between 0 and 1.5 V at a current density of 100 mA g^{-1}, (b) cycling performances of the P/GnP electrodes charged at a current density of 100 mA g^{-1} (with C_{total} and C_p denoting the specific capacity calculated based on the weight of the P/GnP composite and based on the weight of phosphorus alone, respectively), (c) rate capability of the P/GnP composites between 0 and 1.5 V, and (d) comparison of P/GnPs-500 with different reported phosphorus/carbon composites[20,23,24] for sodium ion storage.

Fig. 3(b) shows the cycling performance of the P/GnPs-500 composite charged at a current density of 100 mA g^{-1}. For comparison, the P/GnPs-300 electrode was also tested under the same experimental conditions, and its cycling performance is also shown in Fig. 3(b). C_{total} and C_p denote the specific capacity

calculated based on the weight of the P/GnP composite and based on the weight of the phosphorus alone, respectively. The P/GnPs-300 presents a dramatic capacity decay of 4 mA h g^{-1} per cycle, with a C_{total} of 205 mA h g^{-1} over 100 cycles. In contrast, the P/GnPs-500 composite possessing P–C bonds showed superior cycling stability, with a capacity decay of 0.66 mA h g^{-1} per cycle. 864 mA h g^{-1} and 1234 mA h g^{-1} were retained for C_{total} and C_p over 100 cycles, respectively. Moreover, the coulombic efficiency of the P/GnPs-500 composite increased from 45% to 67%, compared with that of the P/GnPs-300. Even when charged at a current density of 1 A g^{-1}, the P/GnPs-500 electrode still demonstrated excellent cycling performance, with 92.5% retention of the capacity in the second cycle (649 mA h g^{-1}) over 200 cycles, as shown in Fig. S8.† Table 1 summarizes the electrochemical performances of phosphorus and carbon composites as anode materials for sodium ion batteries. Compared with the other red phosphorus and carbon (such as Super P, graphene, and SWCNT) composites reported, the cycling performance of our synthesized P/GnPs-500 composite is superior for sodium ion storage. This is due to the P–C bond formation, leading to a better connection between the red phosphorus particles and the graphene nanoplates, which improves the cycling stability. The structural stability of the P/GnPs-500 composite is also evidenced by the smaller impedance changes in the electrode during cycling, in comparison with the P/GnPs-300 (Fig. S7†). Table S1† shows a comparison of R_{ct} values calculated for the P/GnP composites with and without P–C bonds. After 100 cycles, the R_{ct} value of the P/GnPs-500 composite increased a little, from 95 Ω to 106 Ω, while the R_{ct} value of the P/GnPs-300 composite changed from 147 Ω to 277 Ω. In order to calculate the contribution of red P to the capacity of the P/GnPs-500 composite, we milled natural graphite for 40 h at 500 rpm. The electrochemical performance of the milled graphite is shown in Fig. S9.† The milled graphite delivered first discharge and charge capacities of 388 mA h g^{-1} and 168 mA h g^{-1}, respectively (Fig. S9(a)†). The huge irreversible capacity is due to the SEI formation on the surface of the milled graphite particles, resulting from the electrolyte decomposition. In the second cycle, the milled graphite delivered 186 mA h g^{-1} capacity. According to eqn (1), where 0.3 and 0.7 are the weight fractions of P and graphite in the composite, respectively, the capacity contributed by P is 1558 mA h g^{-1}.

$$0.7 \times C_{phosphorus} + 0.3 \times C_{milled\ graphite} = C_{total} \quad (1)$$

To further explore the structural stability of the P/GnP composites, the morphologies of the P/GnPs-500 and P/GnPs-300 electrodes after 200 cycles were characterized by TEM. The cells were disassembled in an Ar-filled glove box, and photographs of the P/GnPs-500 and P/GnPs-300 electrodes after 200 cycles were taken and are presented in Fig. S8.† Notably, some P/GnPs-300 active materials peeled off from the substrate, while the P/GnPs-500 electrode maintained its integrity even after 200 cycles (Fig. S10†). These photographs provide evidence for the superior cycling stability of P/GnPs-500 over that of P/GnPs-300. Fig. 4(a) shows the morphology of the P/GnPs-300 electrode after 200 cycles. It is clear that the particles of P/graphite-300 are pulverized into isolated nanoparticles due to the huge volume changes in the P during cycling. The high resolution TEM image demonstrates that the size of the pulverized particles was less than 5 nm, as shown in Fig. 4(b). By contrast, the original morphology of the P/GnPs-500 remains its primary morphology, and significant pulverization of particles cannot be observed (Fig. 4(c) and (d)), suggesting that the structure of the P/GnPs-500 is more stable than that of P/GnPs-300. A schematic illustration of the structural evolution of P/GnPs-500 and P/GnPs-300 after cycling is shown in Fig. 5. During the charge–discharge

Table 1 Summary of the electrochemical performances of phosphorus–carbon composites as anode materials for sodium ion batteries

Carbon source	Percentage of P	Voltage range	Mass loading (mg cm^{-1})	1st capacity (based on the composite)	Cycling performance (capacity based on the composite)	Capacity decay (per cycle)	Reference
Single-walled carbon nanotubes	60%	0.001–2 V	0.7–1.2	670 mA h g^{-1} (at a current density of 50 mA g^{-1})	560 mA h g^{-1} over 200 cycles (current density of 500 mA g^{-1})	0.2 mA h g^{-1}	23
Graphene	70%	0–2 V	0.8–1.0	1454 mA h g^{-1} (at a current density of 260 mA g^{-1})	1194 mA h g^{-1} over 60 cycles (at a current density of 260 mA g^{-1})	1.3 mA h g^{-1}	24
Super P	70%	0–1.5 V	2.0–3.0	1323 mA h g^{-1} (at a current density of 143 mA g^{-1})	1230 mA h g^{-1} over 30 cycles (at a current density of 143 mA g^{-1})	3.1 mA h g^{-1}	21
Super P	70%	0–2 V	3.0	1235 mA h g^{-1} (at a current density of 250 mA g^{-1})	700 mA h g^{-1} over 140 cycles (at a current density of 250 mA g^{-1})	3.8 mA h g^{-1}	20
Multi-walled carbon nanotubes	70%	0–1.5 V	—	1547 mA h g^{-1} (at a current density of 143 mA g^{-1})	525 mA h g^{-1} over 20 cycles (at a current density of 143 mA g^{-1})	32 mA h g^{-1}	22
Graphite	70%	0–1.5 V	1.5–2.0	1471 mA h g^{-1} (at a current density of 100 mA g^{-1})	667 mA h g^{-1} over 200 cycles (current density of 500 mA g^{-1})	0.66 mA h g^{-1}	This work

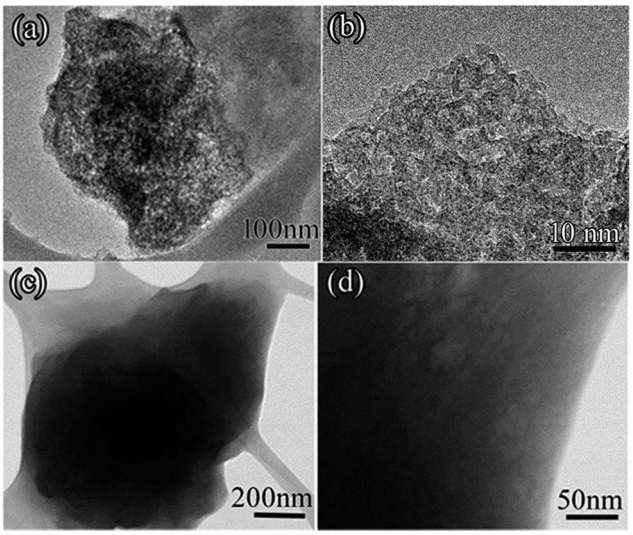

Fig. 4 TEM images of (a and b) P/GnPs-300 and (c and d) P/GnPs-500 electrodes after 100 cycles.

process, the red P particles undergo huge volume expansion and condensation (about 490%), and concomitantly, enormous stresses emerge in the particles, leading to pulverization of the red phosphorus. As a result, some red P particles lose contact with both other red P particles and with the graphene nanoplates, so that the electrical conductivity is reduced. On the basis of our present investigation, the electrical conductivity plays an important role in the reversible capacity and cycling stability of red P.[22] Thus, for the P/GnPs-300 composite, the loss of electrical contact in the active materials leads to capacity decay. In contrast, for the P/GnPs-500 composite, the P–C bonds foster close connections between the P particles and the graphene nanoplates. Moreover, the P–C bond plays a role in restraining the expansion of P particles during the sodiation of P. Even if the P particles are pulverized during the cycling, the red P particles can maintain their contact with the graphene nanoplates, so that good electrical conductivity is retained. Therefore, the P/GnPs-500 composite has excellent cycling stability.

The rate capability of the P/GnPs-500 composite was also investigated at a variety of current densities from 50 mA g^{-1} to 10 A g^{-1} in the voltage range of 0–1.5 V. As shown in Fig. 3(c), the P/GnPs-500 electrode delivered stable capacities of 990, 935, 888, 843, and 788 mA h g^{-1} at the current densities of 50, 100, 250, 500, and 1000 mA g^{-1}, respectively. Even at current densities as high as 5 A g^{-1} and 10 A g^{-1}, the P/GnPs-500 electrode still retained capacities of 413 mA h g^{-1} and 274 mA h g^{-1}, corresponding to a capacity retention of 41.7% and 27.6%, respectively. Then, the current density was returned to the low value of 50 mA g^{-1}, and the capacity was restored to the previous value of 989 mA h g^{-1}, suggesting that the P/GnPs-500 composite has excellent rate capability. By comparison, the capacity of the P/GnPs-300 electrode dropped dramatically with increasing current density. With operation at the current density of 1000 mA g^{-1}, only 75 mA h g^{-1} was retained. On increasing the current density to 2.5 A g^{-1}, 5 A g^{-1}, and 10 A g^{-1}, the capacity delivered by the P/GnPs-300 electrode was nearly zero. In addition, the rate capability of the P/GnPs-500 composite was further compared with that of other P/carbon composites previously reported. Fig. 3(d) shows a comparison of the rate capability between other phosphorus/carbon (SWCNT, Super P®, and graphene) composites and P/GnPs-500 composite for sodium ion storage. It can be clearly seen that the P/GnPs-500 composite presents superior rate capability to other P/carbon composites. This is possibly due to the excellent conductivity of P/GnPs-500 composite as a benefit of the P–C bond formation.

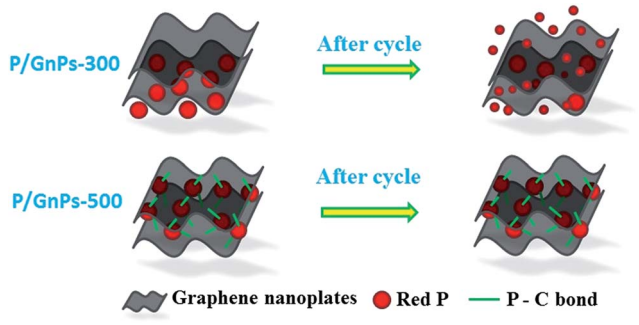

Fig. 5 Schematic illustration of the structural evolution of P/GnPs-500 and P/GnPs-300 after cycling.

4. Conclusion

In summary, we prepared red phosphorus and graphene nanoplates composites by a facile and scalable ball milling method. The SEM and TEM images show that the graphite was exfoliated into nanoplates through the shear forces during the milling process, and the small phosphorus particles were embedded in the graphene nanoplates. Moreover, the XPS results demonstrate the existence of P–C bonds formed between the red phosphorus particles and the graphene nanoplates in the P/GnPs-500 composite. This unique morphology and strong chemical bonding is responsible for the stable structure of the P/graphene composite. During the sodiation of P, the P–C bond plays a role in restraining the expansion of P particles. Moreover, even if the P particles are pulverized during the cycling, the red P particles can remain in contact with the graphene nanoplates, so that good electric conductivity is retained. Therefore, the P/GnPs-500 composite has excellent cycling stability and superior high rate capability, compared to that of the P/GnP-300 composite which does not have P–C bonds.

Acknowledgements

The work is supported by the Australian Research Council through a Linkage Project (LP120200432). The authors would like to also thank Dr Tania Silver for critical reading of the manuscript and Dr Dongqi Shi for XPS testing. We also acknowledge the use of the facilities in the UOW Electron Microscopy Centre and especially thank Dr Gilberto Casillas-Garcia and Chao Han for TEM testing.

Notes and references

1 B. Dunn, H. Kamath and J. M. Tarascon, *Science*, 2011, **334**, 928–935.
2 Z. Yang, J. Zhang, M. C. W. Kintner-Meyer, X. Lu, D. Choi, J. P. Lemmon and J. Liu, *Chem. Rev.*, 2011, **111**, 3577–3613.
3 S. P. Ong, V. L. Chevrier, G. Hautier, A. Jain, C. Moore, S. Kim, X. H. Ma and G. Ceder, *Energy Environ. Sci.*, 2011, **4**(9), 3680–3688.
4 R. Berthelot, D. Carlier and C. Delmas, *Nat. Mater.*, 2011, **10**, 74–80.
5 P. Palomares, P. Serras, I. Villaluenga, K. B. Hueso, J. Carretero-Gonzalez and T. Rojo, *Energy Environ. Sci.*, 2012, **5**, 5884–5901.
6 N. Yabuuchi, M. Kajiyama, J. Iwatate, H. Nishikawa, S. Hitomi, R. Okuyama, R. Usui, Y. Yamada and S. Komaba, *Nat. Mater.*, 2012, **11**, 512–517.
7 M. D. Slater, D. Kim, E. Lee and C. S. Johnson, *Adv. Funct. Mater.*, 2012, **23**, 947–958.
8 H. L. Pan, Y. S. Hu and L. Q. Chen, *Energy Environ. Sci.*, 2013, **6**, 2338–2360.
9 Z. Hu, L. Wang, K. Zhang, J. Wang, F. Cheng, Z. Tao and J. Chen, *Angew. Chem., Int. Ed.*, 2014, **53**, 12794–12798.
10 S. L. Chou, Y. D. Pan, J. Z. Wang, H. K. Liu and S. X. Dou, *Phys. Chem. Chem. Phys.*, 2014, **16**, 20347–20359.
11 S. Li, Y. F. Dong, L. Xu, X. Xu, L. He and L. Q. Mai, *Adv. Mater.*, 2014, **26**, 3545–3553.
12 Y. F. Dong, S. Li, K. N. Zhao, C. H. Han, W. Chen, B. L. Wang, L. Wang, B. Xu, Q. L. Wei, L. Zhang, X. Xu and L. Q. Mai, *Energy Environ. Sci.*, 2015, **8**, 1267–1275.
13 W. J. Li, S. L. Chou, J. Z. Wang, Y. M. Kang, J. L. Wang, Y. Liu, Q. F. Gu, H. K. Liu and S. X. Dou, *Chem. Mater.*, 2015, **27**, 1997–2003.
14 Z. H. Wang, L. Qie, L. X. Yuan, W. Zhang, X. Hu and Y. H. Huang, *Carbon*, 2013, **55**, 328–334.
15 T. Q. Chen, Y. Liu, L. Pan, T. Lu, Y. Yao, Z. Sun, D. H. C. Chua and Q. Chen, *J. Mater. Chem. A*, 2014, **2**, 4117–4121.
16 Y. Liu, N. Zhang, L. F. Jiao, Z. L. Tao and J. Chen, *Adv. Funct. Mater.*, 2015, **25**, 214–220.
17 M. Walter, R. Erni and M. V. Kovalenko, *Sci. Rep.*, 2015, **5**, 8418.
18 M. He, K. Kravchyk, M. Walter and M. V. Kovalenko, *Nano Lett.*, 2014, **14**, 1255–1262.
19 Y. Zhu, X. Han, Y. H. Xu, Y. Liu, S. Zheng, K. Xu, L. Hu and C. S. Wang, *ACS Nano*, 2013, **7**, 6378–6386.
20 J. F. Qian, X. Y. Wu, Y. L. Cao, X. P. Ai and H. X. Yang, *Angew. Chem., Int. Ed.*, 2013, **125**, 4731–4734.
21 Y. Kim, Y. Park, A. Choi, N. S. Choi, J. Kim, J. Lee, J. H. Ryu, S. M. Oh and K. T. Lee, *Adv. Mater.*, 2013, **25**, 3045–3049.
22 W. J. Li, S. L. Chou, J. Z. Wang, H. K. Liu and S. X. Dou, *Nano Lett.*, 2013, **13**, 5480–5484.
23 Y. Zhu, Y. Wen, X. Fan, T. Gao, F. D. Han, C. Luo, S. C. Liou and C. S. Wang, *ACS Nano*, 2015, **9**, 3254–3264.
24 J. Song, Z. Yu, M. L. Gordin, S. Hu, R. Yi, D. Tang, T. Walter, M. Regula, D. Choi, X. Li, A. Manivannan and D. Wang, *Nano Lett.*, 2014, **14**, 6329–6335.
25 I. Y. Jeon, H. J. Choi, S. M. Jung, J. M. Seo, M. J. Kim, L. M. Dai and J. B. Baek, *J. Am. Chem. Soc.*, 2013, **135**, 1386–1393.
26 J. Sun, G. Zheng, H. W. Lee, N. Liu, H. Wang, H. Yao, W. Yang and Y. Cui, *Nano Lett.*, 2014, **14**, 4573–4580.
27 L. Malard, M. Pimenta, G. Dresselhaus and M. Dresselhaus, *Phys. Rep.*, 2009, **473**, 51–87.